Acta Biomaterialia 163 (2023) 117–130

Contents lists available at ScienceDirect

Acta Biomaterialia

journal homepage: www.elsevier.com/locate/actbio

Full length article

Multicellular aligned bands disrupt global collective cell behavior☆

Mahvash Jebeli[a], Samantha K. Lopez[a], Zachary E. Goldblatt[a], Dannel McCollum[b], Sebastian Mana-Capelli[b], Qi Wen[c], Kristen Billiar[a,*]

[a] Biomedical Engineering Department, Worcester Polytechnic Institute, Worcester MA, USA
[b] University of Massachusetts Medical School, Worcester MA, USA
[c] Physics Department, Worcester Polytechnic Institute, Worcester MA, USA

ARTICLE INFO

Article history:
Received 24 May 2022
Revised 10 October 2022
Accepted 19 October 2022
Available online 26 October 2022

Keywords:
Valvular interstitial cell
Collective cell behavior
Microcontact printing
Traction force microscopy
Mechanical stretch

ABSTRACT

Mechanical stress patterns emerging from collective cell behavior have been shown to play critical roles in morphogenesis, tissue repair, and cancer metastasis. In our previous work, we constrained valvular interstitial cell (VIC) monolayers on circular protein islands to study emergent behavior in a controlled manner and demonstrated that the general patterns of cell alignment, size, and apoptosis correlate with predicted mechanical stress fields if radially increasing stiffness or contractility are used in the computational models. However, these radially symmetric models did not predict the existence of local regions of dense aligned cells observed in seemingly random locations of individual aggregates. The goal of this study is to determine how the heterogeneities in cell behavior emerge over time and diverge from the predicted collective cell behavior. Cell-cell interactions in circular multicellular aggregates of VICs were studied with time-lapse imaging ranging from hours to days, and migration, proliferation, and traction stresses were measured. Our results indicate that elongated cells create strong local alignment within preconfluent cell populations on the microcontact printed protein islands. These cells influence the alignment of additional cells to create dense, locally aligned bands of cells which disrupt the predicted global behavior. Cells are highly elongated at the endpoints of the bands yet have decreased spread area in the middle and reduced mobility. Although traction stresses at the endpoints of bands are enhanced, even to the point of detaching aggregates from the culture surface, the cells in dense bands exhibit reduced proliferation, less nuclear YAP, and increased apoptotic rates indicating a low stress environment. These findings suggest that strong local cell-cell interactions between primary fibroblastic cells can disrupt the global collective cellular behavior leading to substantial heterogeneity of cell behaviors in constrained monolayers. This local emergent behavior within aggregated fibroblasts may play an important role in development and disease of connective tissues.

Statement of significance

Mechanical stress patterns emerging from collective cell behavior play critical roles in morphogenesis, tissue repair, and cancer metastasis. Much has been learned of these collective behaviors by utilizing microcontact printing to constrain cell monolayers (aggregates) into specific shapes. Here we utilize these tools along with long-term video microscopy tracking of individual aggregates to determine how heterogeneous collective behaviors unique to primary fibroblastic cells emerge over time and diverge from computed stress fields. We find that dense multicellular bands form from local collective behavior and disrupt the global collective behavior resulting in heterogeneous patterns of migration, traction stresses, proliferation, and apoptosis. This local emergent behavior within aggregated fibroblasts may play an important role in development and disease of connective tissues.

1. Introduction

Morphogenesis, tissue repair, and cancer metastasis are driven by collective cell behaviors which differ substantially from independent cell behavior. Studies that use voids, scratch assays [1–5],

☆ Part of the Special Issue on the Mechanics of Cells and Fibers, guest-edited by Professors Amrinder S. Nain, Derrick Dean, and Guy M. Genin.

* Corresponding author at: Biomedical Engineering Department, Worcester Polytechnic Institute, 100 Institute Road, Worcester, MA 01609.
E-mail address: kbilliar@wpi.edu (K. Billiar).

https://doi.org/10.1016/j.actbio.2022.10.041
1742-7061/

and micropatterned protein "islands" [6,7] in specific geometries [8–12] demonstrate that emergent mechanical stress patterns contribute in large part to the collective cell behavior. In particular, maximum traction stresses at the surface correlate positively with proliferation at pattern edges [13], while the anisotropy of computed cell layer stresses correlate with cell alignment and elongation [14]. The majority of studies on collective cell behavior utilize epithelial cells and cell lines which exhibit relatively uniform cell area when in a monolayer as well as strong contact inhibition. Emergent patterns in the behavior of these cell types are explained relatively well with computational mechanical models that assume uniform cell mechanical properties such as modulus and contractility [9,10,12,15]. However, primary mesenchymal and spindle like cells, which are more contractile and have strong cell-cell interactions, exhibit less uniform behavior when cultured as monolayers [5,16,17].

The complex collective cell behavior of primary valvular interstitial cells (VICs) is implicated in calcific aortic valve disease [18,19]. VICs cultured as monolayers, sheets of cells without any confinement, detach under high tension and form multicellular aggregates which become hyperconfluent. The cells in these high-density regions undergo apoptosis and calcification [18–20]. Previously, we used uniform circular protein islands to form consistent multicellular aggregates, with confined sizes, to study the effects of collective cell behavior on calcification of these cells [21]. We found that the general patterns of cell alignment, size, and apoptosis correlate with predicted mechanical stress fields if nonuniform cell properties are used in computational models [22,23]. However, these radially symmetric models did not predict the substantial heterogeneity in cell behavior observed in individual circular aggregates. In particular, we observed asymmetric apoptotic patterns associated with local hyperconfluent regions. We also observed groups of aligned elongated cells spanning the 200 μm-diameter collagen islands. Similar collective alignment of spindle-shaped cells forming well-aligned nematic domains have been reported in boundary-free monolayers and on circular patterned protein islands by Silberzan and colleagues [17]. In particular, they show the alignment pattern of NIH 3T3 cells and C2C12 myoblasts (both spindle-shaped cells similar to VICs) stabilizes when the cells reach confluence, and on circular protein islands the aligned regions span between two facing "+1/2 defects" located at 2/3 of the radius from the center [17]. In contrast, the groups of aligned VICs in our system terminate closer to the edge and can be observed in many different locations. Further, the VICs do not stabilize in density or size over time in culture, rather they proceed to local hyperconfluency and subsequently detach from the substrate at later timepoints (multiple days) indicating that high traction forces emerge from the collective cell behavior. The observed hyperconfluency of VICs in our model may have importance in the pathology of diseases involving calcification where densification and elevated cell-cell forces are postulated to play critical roles.

The goal of this work is to uncover the mechanisms underlying the observed heterogeneous collective cell behaviors within micropatterned VIC aggregates. Circular stamps are employed to provide a uniform radially symmetric global constraint, and relatively large 400 μm-diameter collagen islands were chosen to minimize the spanning of single cells across the patterns. We use long-term time-lapse imaging to follow the evolution of individual aggregates over four days as substantial heterogeneity between aggregates has been observed even in a single dish of uniformly printed cell islands. Short-term time-lapse is used to observe cell-cell interactions in real time and to quantify cell velocity and traction stresses in distinct sub-regions over the span of hours. To determine if cells act independently or collectively in response to an imposed global stimulus, we cyclically stretch aggregates and quantify changes in orientation and elongation. As Yes-associated protein (YAP) is implicated in mechanosensing in many cell types [24–27], we investigate the relationship between YAP activation and apoptosis stemming from the collective cell behavior. The knowledge obtained from this study provides further insight into how collective cell behaviors drive biological phenomena that are implicated in many developmental and pathological conditions.

2. Methods

2.1. Substrate preparation

Microcontact printed 400 μm diameter circular protein islands were formed by coating plasma-treated and 70% EtOH prerinsed polydimethylsiloxane (PDMS) stamps with collagen and placing them onto untreated 22 × 22 mm square coverslips for 1 h; a 50 g weight was lightly applied to create uniform pressure on the stamp (Fig. S1). The collagen solution consisted of 25 μL of 4 mg/mL collagen, 75 μL of 0.1 M acetic acid, 900 μL sodium acetate buffer, and sodium periodate. Prior to transfer, excess collagen was removed from the stamp using a combination of air drying and nitrogen stream. In a subset of experiments, the uniformity of the circular collagen prints was verified with the addition of 1 μL Alexa Fluor-488 carboxylic acid, succinimidyl ester (A20000, Invitrogen) to the collagen solution for 1 h at room temperature. To determine the effects of island size, we used 200 μm and 600 μm circular patterns in a subset of experiments.

Circular collagen patterns were printed onto polyacrylamide (PA) gels by indirect microcontact printing [21]. Briefly, for each substrate, 50 μL of PA solution (acrylamide:bisacrylamide (Biorad) of percentages of 7.5/0.24 for ∼20 kPa) were pipetted onto an activated coverslip. The coverslips were activated by soaking in 1.5% (aminopropyl) trimethoxysilane solution for 30 min then in 0.5% glutaraldehyde solution overnight at 4°C and dried completely before use. After placement of PA solution on activated coverslips an inactivated collagen microcontact printed coverslip was gently placed on top. Following 12 min of polymerization of the PA-gel, the coverslips were separated by a razor blade. A modulus of ∼20 kPa was chosen because it is in the range of reported stiffness values for healthy and diseased valves [28,29].

2.2. Traction force microscopy

To quantify the shear stresses that the cells apply to the surface of the substrate via traction force microscopy (TFM), 0.2 μm red fluorescent micro-beads were coated on plasma treated glass coverslips, allowed to dry, and then applied to the top surface of the PA gel solution during polymerization. Collagen patterns were then stamped onto the PA gel using direct microcontact printing methods as previously described [30]. At various timepoints, phase and fluorescent images were acquired to determine the aggregate borders and bead locations, respectively. Cells were then trypsinized, and a reference image of the bead locations was acquired. Displacements of the beads were calculated with a custom MATLAB code and input into a finite element model (modulus: 19 kPa; Poisson ratio: 0.4; material property: linear elastic) to calculate the stresses on the surface of the gel (ANSYS Inc.) [30]. To calculate the total traction force of an aligned band, the stresses exceeding a certain threshold in the "hotspots" at the ends of the band were extracted using a custom written MATLAB code. Then the sum of the stresses multiplied times the areas over which they act were calculated and the total force magnitudes for the two opposing hotspots in each aggregate were averaged.

2.3. Dynamic stretching

To determine the effect of cyclic stretching on the collective behavior in aggregates, PA gels were affixed in each well of a 16-well compliant Elastosil culture plate (CellScale), patterned using indirect microcontact printing, and seeded with cells. After 24 h post-seeding, the substrates were stretched 10% uniaxially at 1 Hz for 8 h using a MechanoCulture FX (CellScale). PA gels were attached to the compliant substrate by treating wells with 1.5% (aminopropyl) trimethoxysilane solution for 5 min, drying, and then treating with 0.5% glutaraldehyde solution for 5 min. After removing the liquid, the wells were dried with nitrogen stream, 4 µL of PA were placed at the bottom of the well and covered with a collagen patterned circular 5 mm coverslip. The wells were then transferred to a vacuum chamber filled with nitrogen for 45 min to facilitate polymerization, then diH_2O was added to the wells for 30 min to promote detachment of the coverslips from the PA gel surface.

2.4. Cell culture and media

Aortic VICs were isolated from porcine hearts obtained from a local abattoir (Blood Farm, Groton, MA) using previous protocols [31]. Porcine VICs are primary fibroblastic cells and were chosen as VIC aggregation is implicated in the pathology of CAVD, in addition to their similarity to human VICs. VICs at passages 3-6 were seeded at 12,500 cells/cm^2 [21]. In one set of experiments, neonatal human dermal fibroblasts (courtesy G. Pins, Worcester Polytechnic Institute) were used with the same passage range, cell density, and culture conditions as VICs. The cells were cultured in DMEM supplemented with 10% FBS and 1% Antibiotic/Antifungal at 37°C with 10% CO_2. Media were exchanged every 48 h. In cell-cell interaction inhibition experiments, calcium was depleted from DMEM with 1 mM ethylenediaminetetraacetic acid (EDTA), a concentrated reported to not affect cell viability [32].

2.5. Stable YAP-VIC cell line

To determine if apoptosis is YAP-dependent, YAP-6A, a constitutively active version of YAP that cannot be inhibited by LATS, was obtained from Addgene (#42562), packaged into lentivirus particles, and transduced into VIC cells. Lentiviral particles were generated by transfecting 293T cells with pLX304-YAP-S6A-V5, pSPAX.2, and PMD2.G. After 48 h, the supernatant was collected and filtered through a 45 µm sterile filter. Viral supernatant was then mixed 1:1 with culture media, added with 1 µg/mL of polybrene (Millipore), and incubated with VICs overnight. The next day, cells were fed with culture media, and after 24 h, cells were selected with 1 µg/mL of Puromycin until all control (uninfected) cells died after approximately 48 h. Expression of the YAP S6A-V5 construct was visualized in pooled puromycin-resistant cells through immunofluorescence using anti-V5 (Invitrogen).

2.6. Imaging and immunohistochemistry

Individual aggregates were tracked for four days utilizing a motorized stage and automated position tracking software (Zeiss Axiovision 4.8.2 SP1) on an inverted microscope (Axiovert 200M, Zeiss) and imaged with phase contrast every 24 h at 10x (AxioCam MRm camera; 1.4 MP, 1388 × 1040 pixels). To track individual aggregates at specific locations, coordinates of each aggregate were saved with respect to a reference point at the top left corner of the coverslip on each day. Samples were incubated for 30 min in standard media with CellEvent Caspase 3/7 (1:400, C10423, Invitrogen) prior to imaging to observe apoptosis. To quantify cell death in long time lapse imaging experiments > 24 hs, propidium iodide (1:100, P1304MP, Invitrogen) was added to the samples 30 min prior to imaging.

YAP staining was completed following published methods [33,34]. VIC aggregates were fixed in 4% paraformaldehyde for 45 min at room temperature, rinsed twice in PBS, and permeabilized using 0.1% TritonX-100 in PBS for 1 h. Samples were then blocked with 5% bovine serum albumin (BSA) overnight at 4°C to minimize nonspecific protein binding. Samples were stained with Anti-YAP in 5% BSA (1:250, mouse, sc-398182, Santa Cruz) primary antibody and incubated for 1 h at room temperature. Samples were rinsed in PBST (0.5 wt% Tween-20 in PBS) two times for 10 min following incubation with primary antibody. Samples were then incubated in secondary antibody with goat anti-mouse AlexaFluor 647 (1:200, A21241, Invitrogen) while counterstained with Alexa Fluor 488 Phalloidin (1:100, A12379, Life Technologies) to visualize F-actin and Hoechst 33342 (1:200, H3570, Life Technologies) to visualize nuclei in 1% BSA for 1 h at room temperature. Samples were rinsed three times for 10 min with PBST, mounted, and imaged using a BioTek Cytation Gen5 inverted microscope. To quantify YAP activation, the colocalization of YAP and Hoechst signals was quantified as nuclear, nuclear/cytoplasmic, or cytoplasmic in the hyperconfluent bands identified in phase images.

To visualize migration of individual cells within the aggregates, 20% of cells were treated with CellTracker™ Green CMFDA Dye (5:1000, C2925, Invitrogen) and imaged via fluorescence microscopy (Axiovert 200M, Zeiss). Only staining a portion of the cells is required so that individual cells can be tracked when cells become dense. To calculate the mean squared distances (MSD), we manually tracked the coordinates each cell's centroid on each frame using ImageJ and calculated the square of the distance moved. To visualize the coordinated movement of cells in hyperconfluent aggregates, we performed particle image velocimetry (PIV) analysis using the PIV tool in ImageJ.

To visualize if the collagen island remained after aggregates detached, a subset of samples was fixed and stained with picrosirius red/fast green (120M1516V, Sigma-Aldrich) and imaged with transmitted light and color camera (Cytation 5, BioTek).

To quantify proliferation, Click-iT™ Plus EdU Cell Proliferation Kit for Imaging, Alexa Fluor™ 488 dye was used per manufacturer's instructions (C10637, Invitrogen). We performed both a 24 h-long exposure to visualize proliferation over an entire population doubling and a 1-hr pulse experiment for short-term visualization with minimal migration away from the site of proliferation.

2.7. Quantification of confluency level, cell density, and cell alignment

To quantify the observed confluency levels in each aggregate, the area of the cells in phase images was measured using ImageJ and divided by the total area of the collagen island in the same image. To quantify the average density of cells in different confluency levels, the number of the cells in each aggregate was divided by its area.

To qualify the orientation of aligned cell regions from phase images, the aggregates were analyzed with the OrientationJ plugin in ImageJ to produce color orientation maps. To calculate the percentage of aligned area, we divided the size of the local aligned area (i.e., area with the same color) by the total area of the aggregate.

To quantify the alignment of cells in live cultures before and after stretch, F-actin was stained using CellMask™ Actin Tracking at 1:1000 dilution (A57249, Invitrogen). As this staining of live cells is not as efficient as phalloidin staining of fixed and permeabilized cells, only a portion of the cells are stained brightly. Further, imaging through the 400 µm-thick silicone well and the ~200 µm-thick PA gel degrades the quality of the images. Together, these limitations make quantification of the stress fiber angular distribution problematic; however, as individual cells could be identified

clearly, we were able to track these individual cells before and after stretch and quantify their direction and elongation by tracing each stained cell and calculating the angle and elongation of the stained fibers with the Directionality tool in ImageJ.

2.8. Statistical Analysis

Data are presented as mean and standard deviation. One-way ANOVA was performed to evaluate the significance of cell density values between the five different confluency levels. Two-way ANOVAs were used to assess the significance of cell location (inside/outside of bands), and inter-aggregate variability on YAP nuclear localization and separately on proliferation. Holm-Sidak post-hoc tests were used for pairwise comparisons. Student's t-test was used to evaluate the significance in differences of cell speed between confluent and hyperconfluent regions. Paired t-tests were used to evaluate of the significance of changes in the cell orientation and aspect ratio before and after stretch and to compare apoptosis levels of YAP activated and control cells. Analyses were completed in SPSS, and a p-value of less than 0.05 was considered statistically significant.

3. Results

3.1. Aggregates have variable rates of progression towards confluency

Across the span of 4 days, 53 aggregates were tracked following initial seeding. On the 400 μm-diameter collagen islands containing 50-300 cells, cells migrate, proliferate, and fill the islands at varying rates. As the density of cells was variable within each aggregate, we manually categorized aggregates in terms of confluency level and measured the percentage of the island area that is covered with cells (Fig. 1A). In the "sparse" stage, relatively large regions of islands are visible between cells and coverage is 80.0±9.0%. In the "preconfluent" stage, cells fill most of the circular area (89.6±5.1% coverage) and only small areas of the surface are visible. At the "confluent" stage, cells cover almost the entire area (95.6±1.7% coverage), and cell density is approximately uniform. The "hyperconfluent" stage is characterized by regions in which cells are highly dense and rounded, although there are still small gaps in some aggregates (97.3±0.8% coverage). In the "self-detached" stage, highly dense areas are formed when portions of the aggregate pull away from the culture surface. The average cell density correlates with the confluency level (Supplemental Fig. S2A), although there is not a one-to-one correspondence due to the heterogeneity within each aggregate e.g., some aggregates with highly dense regions are categorized as hyperconfluent yet have an average cell density in the confluent range.

To account for potential inconsistencies in initial seeding, we set the preconfluent level to be "time zero." Despite this data shift, we still observe substantial variability in how long it takes aggregates to progress through confluency levels (Fig 1C). The majority of aggregates progress from preconfluent to confluent within 12 h (as indicated by the thickness of the line). Note that the aggregate shown in Fig. 1A corresponds to a line in Fig. 1C where every 24 hours the level of confluency moves one higher. Rather than seeding density, it appears that banding plays a predominate role in variability in timing. Aggregates with a high area of alignment (>30% on average) of the cells in sparse level on Day 1 detach by Day 4, whereas those with a lower percentage area aligned (>20% on average) do not. The percentage of area aligned is significantly higher in the prior group on each day of culture (ANOVA, $p < 0.05$; Supplemental Fig. S2). These multicellular bands can be observed more clearly in phase imaging following fixation when individual cells separate due to the dehydration process, and fluorescent staining shows continuous F-actin structures spanning regions with high numbers of nuclei (Fig. 1D).

3.2. Local hyperconfluency occurs following band formation

Despite the simple circular shape of the collagen islands, few aggregates had the expected radially symmetric patterns with circumferential alignment at edges and isotropic cells in the center (see Fig 2A right column for example). Even these relatively symmetric aggregates (e.g., Fig. 2A, 4th column) exhibit short regions of aligned cells at intermediate timepoints (Fig. 2A, 2nd and 3rd columns) which become hyperconfluent in the central region but do not span the entire aggregate and thus do not self-detach. In most aggregates, multicellular banding was observed disrupting the radial symmetry, even at early timepoints (Fig. 2B left panels). After 4 days of culture, pronounced hyperconfluent bands were observed in all aggregates (Fig. 2B right panels). If banding is pronounced at the preconfluent stage (Fig. 2C left panels), the band becomes highly dense within 24 h and leads to self-detachment of cells from the substrate at the two endpoints of the banded region (Fig. 2C right panels, Fig. S2F).

In the majority of aggregates, bands form a straight line from one edge of the aggregate to the other. Less often the bands are curved, only span a small internal region, or connect into triangular patterns (Supplemental Fig. S3). Most bands eventually lead to some degree of self-detachment within the 4-day culture period.

3.3. Banding occurs regardless of aggregate size

In previous studies, we microcontact-printed 200 μm-diameter protein islands and observed VICs forming confluent aggregates with cells generally oriented circumferential at the edges but highly heterogeneous orientation and cell area in the central region [22]. In this study, we used 400 μm-diameter to minimize the "edge effect," yet we still observed highly heterogenous structures within most aggregates. To further lessen the proximity to the edges, 600 μm-diameter islands were created, and similar hyperconfluent bands formed in these large aggregates as well (Fig. 3). This finding, in conjunction with our time-lapse studies where cells aligned with individual elongated cells in aggregate centers, indicates that bands are not forming by cells interacting with the edges. To determine if this behavior is unique for VICs, we cultured primary human dermal fibroblasts on 400 um islands, and we observed similar banding and hyperconfluency (Supplemental Fig. S4).

3.4. Cells migrate to connect with bands and then move in coordination

To better understand how cell migration plays a role in band formation, we performed 4.5 h time-lapse imaging of aggregates with approximately 20% of cells fluorescently labeled so that individual cells could be tracked. Following 162 cells, we observed that cells in relatively sparse regions moved independently, whereas cells within bands moved coherently (Fig. S5). The vast majority of cells (~96%) remain within their respective regions (sparse, band, or edge) over the 4.5 hours (Supplemental Movie M.1). Five cells in sparse regions merged with bands and one cell joined a band from the edge. Four cells from relatively sparse regions joined the ring of aligned cells along the edge in the absence of any band. The behaviors of cells in different regions were qualitatively different; the cells in sparse regions migrated relatively independently whereas the cells in hyperconfluent regions oscillated in sync. Quantitatively, the mean squared displacement is lower in the hyperconfluent regions than the less confluent regions (Supplemental Fig. S6), yet the average speed in less dense regions (8.2 ± 0.8 μm/h)

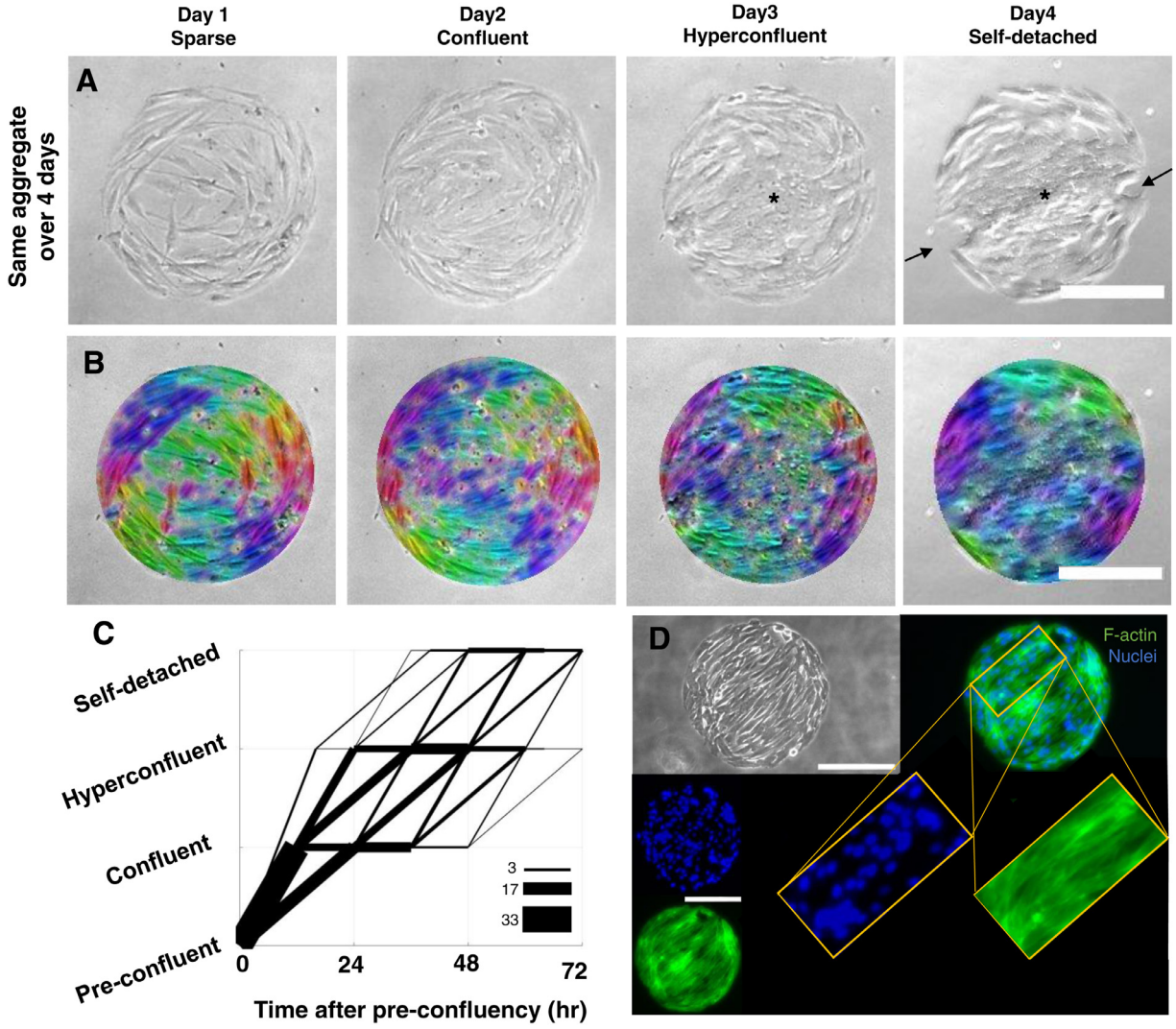

Fig. 1. The progression between levels of confluency varies in time from aggregate to aggregate. A) Time-lapse of the same aggregate over 4 days showing the evolution of its confluency starting sparce 24 h after seeding, proceeding to confluent at day 2, hyperconfluent on day 3 (* indicates high density region), and finally self-detachment on day 4 (arrow indicate regions detached from substrate). B) Orientation analyses by OrientationJ in ImageJ show the progression of aligned areas across an aggregate. C) Plot of levels of confluency versus time adjusted to time when each particular aggregate reached the preconfluent level to remove variability in initial seeding in a single dish ($n = 53$ aggregates; thickness of lines indicates number of aggregates following a given path as indicated in the legend). The majority of aggregates take 12 h to reach confluency, yet there remains high variability in confluency rates from preconfluent to higher levels of confluency after removal of heterogeneity in initial seeding (see other examples in Fig. 2 and Supplemental Fig. S2). D) Local clustering of aligned cells forms banding and hyperconfluent regions. F-actin staining (green) shows the direction of the band, and high density of nuclei (blue) demonstrates hyperconfluency. The phase image in panel D (gray) was captured after fixation and permeabilization which creates spaces between cells not seen in live imaging in panel A. Scale bar = 200 μm.

is not significantly different than in hyperconfluent regions (7.1 ± 1.5 μm/h, t-test, $p = 0.07$).

To understand the events leading to band formation, we imaged aggregates every 30 minutes over 24 hours. Cells under lower confluency levels display a fluid-like behavior with edge cells rotating around the circumference and internal cells beginning to align to one another and forming bands, shown by orientation analysis by OrientationJ (Supplemental Movie M.2A). As confluency progresses, motility within aggregates decreases and cell migration is relatively uncoordinated (Supplemental Movie M.2B). Finally, during hyperconfluent stages, cells move back and forth together with limited migration similar to an oscillation (shown by PIV analysis in Supplemental Movie M.2C). Cell proliferation is observed in the phase images at all confluency levels with less proliferation in hyperconfluent regions. Propidium iodide staining at the beginning of time-lapse experiments suggests that a small amount of apoptosis occurs throughout sub-confluent and confluent aggregates, whereas the extent of cell death is much higher in the middle of hyperconfluent bands. The propidium iodide signal dissipates with time due to photobleaching so is only seen at the early timepoints.

3.5. Proliferation occurs throughout aggregates but decreases in hyperconfluent regions

In contrast to studies showing proliferation of cells predominantly at the edges of constrained epithelial cell monolayers [10,25,35,36], we observe proliferation throughout our confluent aggregates. Images from 1 h EdU pulse experiments show no distinct radial pattern of proliferation (Fig. 4A) even when images of positive cells from multiple aggregates are binarized and stacked (Fig. 4B). The 24 h EdU exposure experiments further indicate less proliferation in hyperconfluent bands (Fig. 4D, 4E).

A two-way ANOVA was performed to analyze the effect of region (hyperconfluent or other regions) and heterogeneity between aggregates (treating aggregates as separate realizations) on

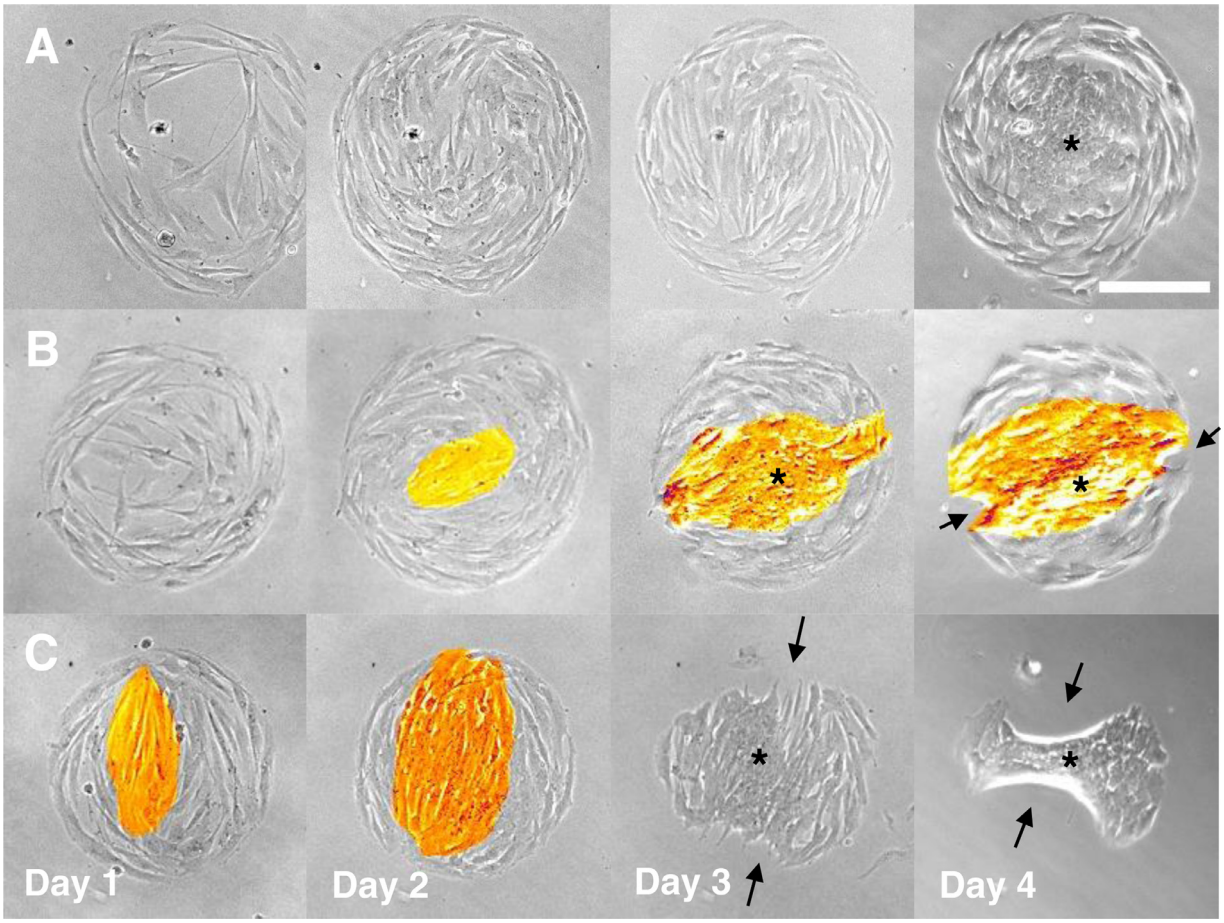

Fig. 2. Three examples of different time courses of confluency progression in aggregates. A) Aggregate with relatively uniform cell distribution exhibiting circumferentially aligned cells around the edge and high density in the center by day 4 but no banding or self-detachment. B) Aggregate with formation of band starting day 2 and leading hyperconfluency by day 3 and slight self-detachment by day 4. C) Aggregate with banding occurring early which proceeds to hyperconfluency and self-detachment by day 3. Banding of aligned cells is highlighted in orange color, * indicates high density region, and arrows indicate regions detached from substrate. Scale bar = 200 μm.

proliferation. The proliferation rate is significantly lower in the hyperconfluent region than other regions ($p = 0.02$, df = 1, F value = 50.6). There were no significant differences between aggregates ($p = 0.91$).

3.6. Local hyperconfluency is inhibited by depleting calcium

To test whether band formation is driven by intercellular force transmission, we decreased cell-cell adhesion by precipitating calcium from the cell culture medium. After four days in culture, the last two of which were in calcium-free media, hyperconfluent regions did not form, and we did not observe any self-detachment (Fig. 5B). The concentration of cells is approximately 1080 cells/mm^2, which falls in the category of preconfluent to confluent as shown in Fig. S2A. However, local regions of cell alignment were still observed. This local alignment may have been established in the first two days of culture in standard medium (Fig. 5A) which is necessary for forming aggregates as proliferation is calcium dependent [37]. When the EDTA was added 24 h post seeding, some of the cells in the middle remain aligned; however, the confluency did not progress within the 4 days of the experiment (Fig. 5C), thus this earlier depletion of calcium was not used for the final experiments.

3.7. Hyperconfluent bands increase local traction forces

Unlike traction stress maps for homogeneous aggregates in which the traction is high and relatively uniform at the edges [10], we observe that the bands accentuate the traction stresses at their endpoints (Fig. 6). When aggregates are preconfluent, traction "hot spots" are relatively low then become much higher when large hyperconfluent bands form. For example, for the representative preconfluent aggregate shown in Fig. 6A & B, the total traction force at the end of the band is 21.3 μN (averaged between the two hotspots) compared to 118.0 μN for the band in the representative hyperconfluent aggregate shown in Fig. 6C & D. Analysis of the principal stress vector directions indicate that stresses are highly anisotropic and predominantly in the direction of bands (Fig. 6 insets 1-4; full vector fields are provided in Supplemental Fig. S6). Time-lapse traction stress maps show that stresses dynamically change in magnitude and location over 4.5 h with cell movement, but peak traction stresses remain at the band ends (Supplemental Movie M.3). Loss of ECM staining in detached regions (Supplemental Fig. S7) indicate that the high traction stresses at the ends of the bands lead to self-detachment by exceeding the strength of the collagen-PA substrate bond/entanglement.

3.8. Cytosolic YAP indicates low tension in hyperconfluent bands

Despite measurement of high traction stress at the ends of the bands, biological markers consistent with a low stress environment such as high cell density, low spread area, and apoptosis indicate low tension within the hyperconfluent bands. As an indirect measure of cell stress, we stained for YAP, a mechanosensitive protein which is shuttled preferentially to the nucleus under high tension

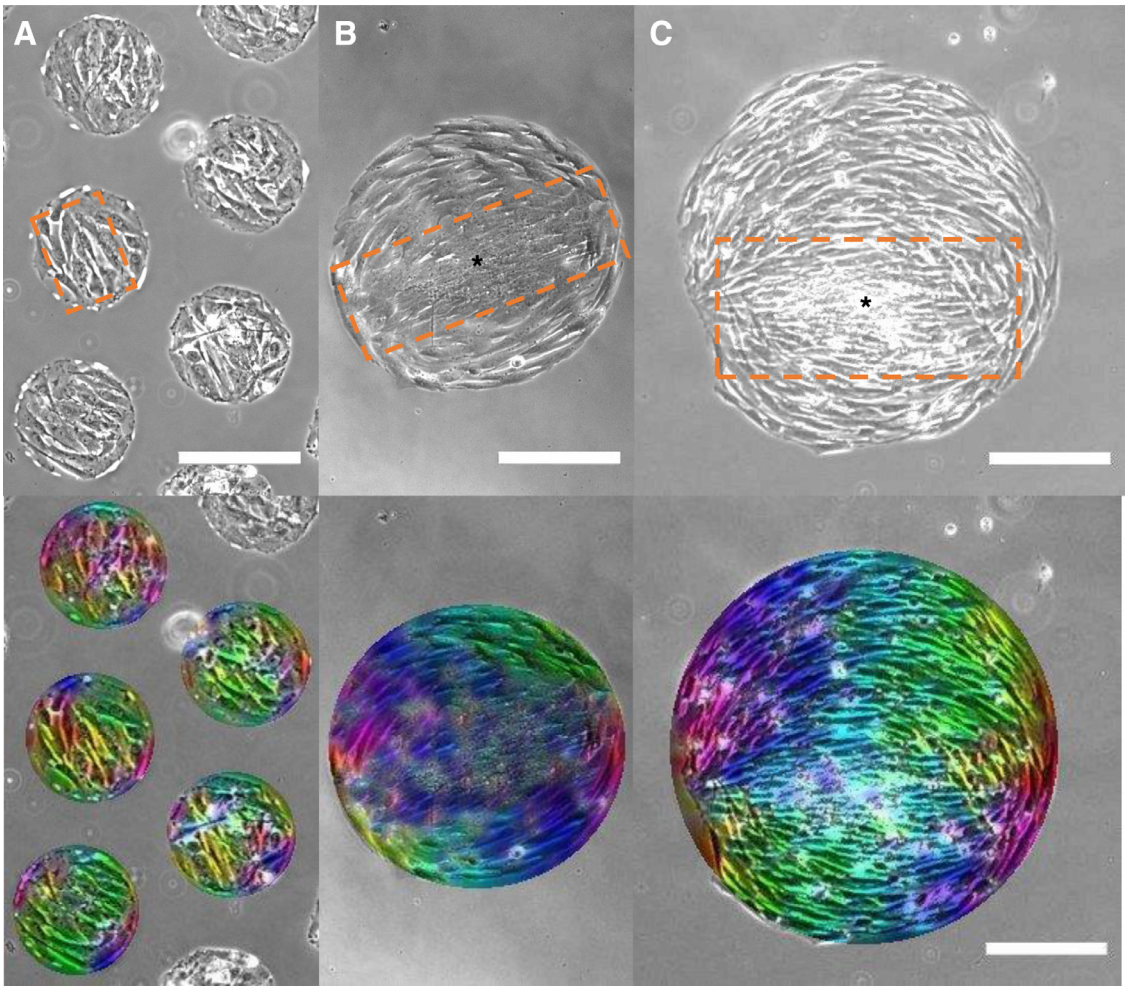

Fig. 3. Banding and hyperconfluency occurs independent of aggregate size as observed in A) 200 μm, B) 400 μm, and C) 600 μm day 4 aggregates. Banding is highlighted by dashed orange rectangle and * indicates high density region. Lower panel show the orientation analysis by OrientationJ in ImageJ. Scale bar = 200 μm.

and remains cytosolic in low tension environments [25]. In our aggregates, cells inside of bands have more cytosolic YAP (Fig. 7B, inset 1) compared to cells outside of bands, which have more nuclear YAP (Fig. 7B, inset 2). At band endpoints, where cells are more elongated, YAP is predominantly nuclear (Fig. 7B, inset 3). We did not observe any purely cytosolic YAP.

Quantification of nuclear (N) and nuclear/cytosolic (N/C) YAP in the center, end of bands, and non-banded regions was performed for four confluent aggregates (Fig 7.C). There was no purely cytosolic YAP observed. The remaining 37 stained aggregates had pronounced hyperconfluent bands in which this analysis was not possible due to difficulty in distinguishing individual nuclei. A two-way ANOVA was performed to analyze the effect of the region with respect to bands and heterogeneity between aggregates (treating aggregates as separate realizations) on YAP deactivation. The YAP nuclear localization is significantly lower in the central region ($p = 0.001$, df = 2, F value = 24.4). There are no significant differences between different aggregates ($p = 0.24$).

3.9. Apoptosis increases in high density regions in a YAP-dependent manner

As reported above, in time-lapse videos with PI staining (Supplemental Movies M.2A, B, C), we observe a low incidence of cell death throughout aggregates except within hyperconfluent regions. We confirmed that this cell death is likely due to apoptosis by staining for cleaved caspase 3/7. Within the first 24 h after preconfluency, approximately 20% of aggregates show a caspase positive signal indicating apoptosis. Most caspase-positive aggregates are confluent aggregates as few hyperconfluent aggregates are present at this time (Fig. 8). At 24-48 h after preconfluency, almost half of the aggregates show caspase activity, and most of these aggregates are hyperconfluent. At 48-72 h after preconfluency, nearly all aggregates show a positive caspase signal with the majority having detached from the surface.

As cytosolic YAP is not observed in sparse regions with low prevalence of apoptosis, we sought to determine if YAP activation (i.e., translocation to the nucleus) is sufficient to inhibit apoptosis. We stably expressed activated YAP in VICs and cultured them on circular collagen islands until hyperconfluent (but prior to self-detachment). Compared to control VICs (Fig. 9A), we observe a dramatic decrease in apoptotic activity in VICs with constitutively active YAP (Fig. 9B). The observed decrease is statistically significant (paired t-test, $p < 0.001$).

3.10. Cells in bands reorient towards stretch but not completely

To examine the response of cells to external loading, we applied 10% cyclic uniaxial stretch for eight hours at 1 Hz frequency. Due to the heterogeneity of band locations, we tracked 38 individual aggregates before and after stretch rather than averaging overall cell behavior between aggregates. Actin fibers were observable with a live stain taken up by cells and imaged in compliant stretch wells without fixation; thus, since not all cells were stained equally, we

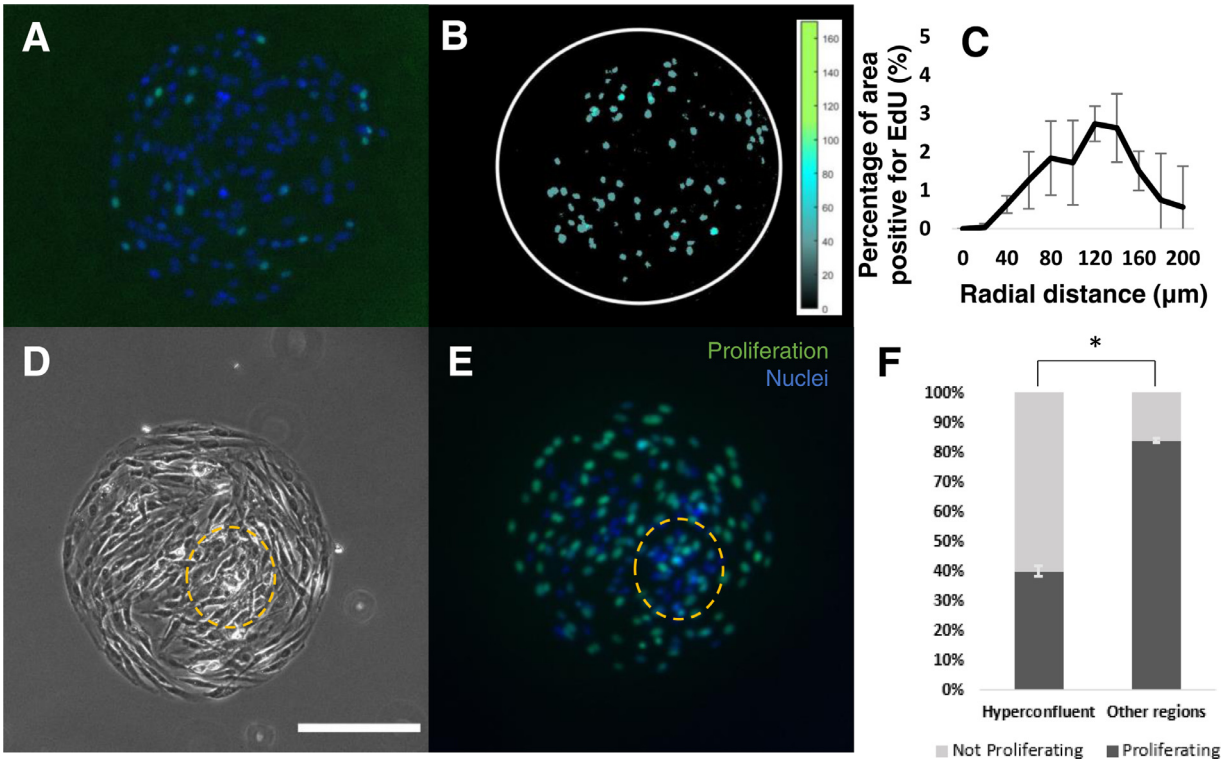

Fig. 4. Proliferation occurs throughout confluent aggregates and less in high-density regions. A) Representative aggregate after 1 h pulse staining for proliferation with EdU. B) Overlay of binarized images of proliferation for 4 different aggregates after 1 h EdU pulse shows proliferation throughout confluent aggregates. C) Frequency of proliferation averaged over 4 aggregates at specific radii shows proliferation is not limited to the edge. D) Representative phase image of a fixed and permeabilized aggregate with a hyperconfluent region (orange outline). E) After 24 h EdU exposure, proliferation occurs throughout the aggregate but is less prevalent in hyperconfluent region. F) In the hyperconfluent regions, the proliferation is significantly lower than the other regions (two-way ANOVA $p = 0.02$, $n = 599$ cells from 3 aggregates). Fluorescent images are merged Hoechst (blue) and EdU (green) images. Scale bar = 200 μm.

manually tracked and quantified the morphology of 56 individual cells within those aggregates before and after stretch.

In general, the cells reorient towards the direction of stretch but are not able to completely reorient to the stretch axis, and the extent of cell reorientation depends upon initial angle of the bands. For cells inside bands originally aligned within ±15° of the direction of stretch (Fig. 10A, circled cells), the alignment of the cytoskeleton becomes more pronounced, and the cells do not reorient in a detectable manner (from 5.2°±7.9° to 2.7°±3.2°, p=0.45, n=9). The aspect ratio of these cells in the direction of stretch increases significantly from 3.7±1.4 to 6.3±3.2 (p=0.04). When bands are at a moderate angle (15° to 45°) relative to the stretch direction, cells reorient significantly towards the direction of stretch but not fully, from 28.0°±13.2° to 18.4°±13.8° (p=0.001, n=23), and aspect ratio trends higher from 2.5±0.7 to 3.0±1.3, but the change is not significant ($p = 0.53$) (Fig. 10B, Supplemental Fig. S10A). When bands are at a large angle relative to the stretch direction, initially at 45° to 90°, a subset of cells reorient towards the stretch direction significantly from 59.1°± 8.8° to 30.0°±18.3° (p=0.003, n=9), whereas in others the cytoskeleton is disrupted, and the cells appear more rounded and the orientation was not quantified (Fig. 10C, Supplemental Fig. S10B).

Cells on island edges that align with the global circular constraint and are in the direction of stretch (top and bottom of the images) are relatively stable and do not reorient in a detectable manner (from −2.5°±16.0° to 1.8°±12.0°, p=0.30, n=16). Conversely, for cells that align to the edges that are perpendicular to the stretch (left and right sides of the images), the cytoskeletons are disrupted thus the reorientation of the perpendicular cells could not be quantified (Fig. 10B, 10C); this cytoskeletal disruption was observed in 20 of the 24 tracked aggregates where perpendicular cells were observed at the edges at prestretch.

4. Discussion

Collective cell interactions drive distinct spatial patterning of cell behavior in monolayers of cells within confined geometries. These emergent patterns correlate strongly with predicted mechanical stress fields indicating a regulatory role of mechanics. Here, we extended studies conducted primarily on epithelial monolayers to more contractile and less contact inhibited primary fibroblastic cells. We analyzed the evolution of VIC confluency on circular micropatterned protein islands over a period of days, a long duration which is relevant for disease modeling. We aimed to determine how observed heterogeneities in spatial patterning are influenced by interactions between neighboring cells and under the influence of the circular global constraint to determine the relative effects of local and global collective behaviors. In contrast to previous reports of radially symmetric cell alignment, proliferation, and differentiation of epithelial cells and cell lines in circular and annular patterns [6,7,9,35], we observe that primary porcine VICs and human dermal fibroblasts align locally and form hyperconfluent bands spanning the circular patterns due to local cell-cell interactions, and this local alignment occurs regardless of pattern diameter (200-600 μm).

The banding behavior bears similarity to local collective behaviors reported in unconstrained fibroblast monolayers from a variety of sources [38–40]. VICs, like other spindle-shaped cells, evolve from a roughly isotropic state to an aligned nematic state as they proceed from sparce to confluent in 2D culture. Well-ordered nematic domains are disrupted by topological defects at high cell density and, when cultured on circular islands, create bands that span the majority of the diameter [17]; however, in contrast to cell lines such as NIH 3T3 and C2C12 cells [17], VICs form bands that can terminate closer to the edges of the patterns than predicted

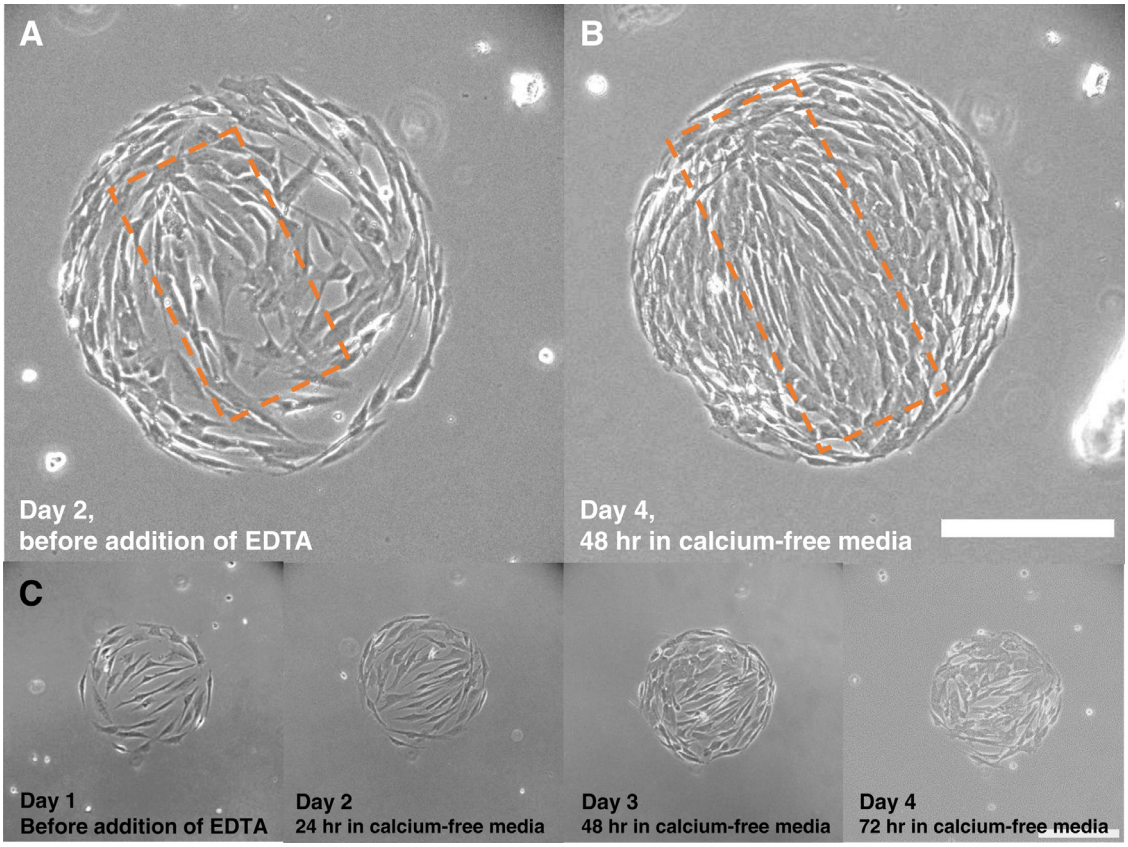

Fig. 5. Inhibiting cell-cell adhesion via calcium depletion prevents hyperconfluency, although banding is still observed. A) A day 2 aggregate before the addition of EDTA (1 mM) shows prealignment of the cells. B) The same aggregate on day 4 after 2 days in a calcium-depleted medium shows aligned cells in a band; however, the cells are not tightly contacting, and hyperconfluent regions are absent. The dashed orange rectangle highlights banding. C) Representative image of an aggregate with the addition of EDTA 24 hs post-seeding. No confluent aggregates were observed after 4 days of culture with this treatment; however, alignment of the cells in the middle remains. Scale bar = 200 μm. For control images, see Fig. 1 as the conditions of the experiments for Fig 1 and Fig 5 are the same with exception on EDTA addition.

for these characteristic defects, possibly due to the large size of the VICs relative to the pattern size and myofibroblast-like contractile behavior. More importantly, VIC and HDFs proceed to local hyperconfluency that is not predicted by the physics and nematic domains or observed for the cell lines, likely due to lower sensitivity to contact inhibition for these primary cells. The formation of hyperconfluent regions has biological ramifications in diseases involving increased rates of proliferation and apoptosis.

The asymmetric locations of bands largely explain the variability in patterns of proliferation, migration, and density observed in these aggregates. The formation of these highly aligned multicellular bands soon after seeding is correlated with self-detachment within 4 days of culture resulting in aggregate-to-aggregate heterogeneity within a single dish of identical collagen islands. Self-detachment and further nodule formation have been induced and studied in the context of dewetting behavior of the epithelial cells [41]. Dewetting is affected by E-cadherin adhesion, which influences the tissue mechanical properties and forces that later could alter the shape of the confined sizes aggregates, e.g., self-detachment [41]. In the current study, self-detachment was the endpoint of our analysis, and we did not investigate further into nodule formation. These observations, along with traction force and time-lapse migration measurements, indicate that VICs exhibit strong local collective behavior that disrupts the emergent behavior emanating from the circular constraint of the islands. Such regional changes in cell shape, number, and confluency should be considered in the mechanical analysis of multicellular systems, especially for primary fibroblastic cells.

Non-uniform stress fields that emerge from transmission of forces between cells have been postulated as the driver of cell alignment and collective behavior in constrained cell islands [9,10,35]. In contrast, our short-term (4.5 h) time-lapse imaging shows that the cell alignment that drives the formation of bands is initiated by a few local cells migrating to and aligning with highly elongated spindle-shaped cells. Rather than acting individually until confluent as seen in epithelial cells [42], VICs often align with each other within the patterns at the preconfluent stage. This local collective behavior may occur due to cells sensing the anisotropic displacement of the underlying PA gel generated by the cell [43] and/or by contact guidance provided by adjacent elongated cells. This behavior occurs regardless of aggregate size up to 600 μm diameter indicating that the banding is not formed due edge effects, i.e., cells do not attach to two points on the circular edge and elongate to span the island. We show that the banding also occurs with primary dermal fibroblasts. Sun and colleagues report that primary rat embryonic fibroblasts align radially at the edge of similar protein islands, and the central cells are smaller and more dense than edge cells, although without banding [16]. This heterogeneous morphology is stark contrast to the patterns observed for NIH3T3 and osteoblast-like MC3T3-E1 cell lines which exhibit uniform spread area throughout the constrained monolayers and circumferentially aligned cells at the edges and less elongated cells in the center [7,16]. Together, these results indicate that for the relatively large and contractile primary fibroblastic cells studied herein, the strong local collective behavior disrupts the global circular constraint that drives the radially symmetric emer-

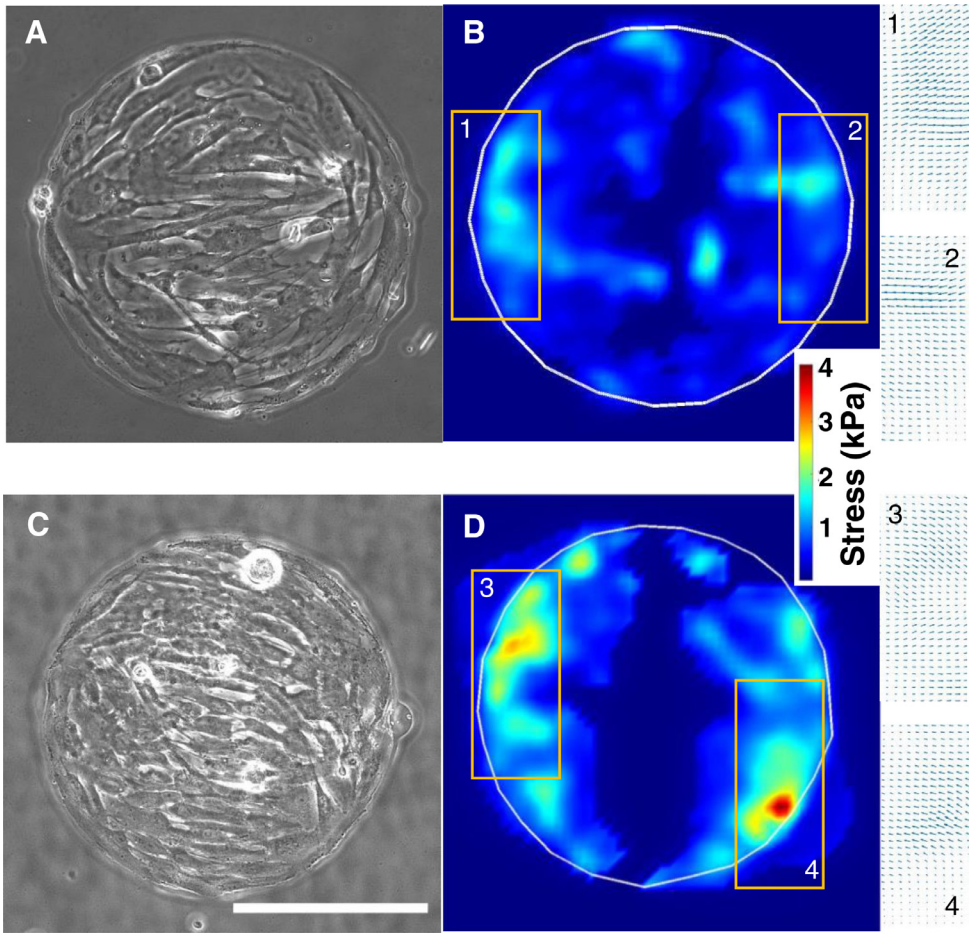

Fig. 6. Heterogeneous traction stress fields are produced by alignment and banding of cells and peak stresses increase with cell density. A) Phase image of a preconfluent aggregate shows initial alignment of cells. B) TFM analysis of the preconfluent aggregate shows low magnitude stress hotspots at ends of aligned cells with inward direction of applied stress (insets 1 & 2). C) Phase image of a hyperconfluent aggregate shows strong banding. D) TFM analysis of the hyperconfluent aggregate shows high magnitude stress hotspots with inward direction of applied stress (insets 3 & 4). Scale bar = 200 μm.

gent collective behavior of other cell types cultured on circular patterns.

The long-term (24 h) time-lapse videos clearly show that even when hyperconfluent, confined VIC cell layers are not static or "jammed" as observed for high-density epithelial monolayers [44–46]. We observe synchronized circumferential collective migration at the edges of preconfluent and confluent VIC aggregates as well as substantial collective movement in the center along the multicellular bands. Similar collective cell migration is observed in epithelial monolayers on small (100-200 μm) circular islands, and vortices of local collective migration are observed in the central regions of larger islands (500-1000 μm) [42]. The average cell speed was not significantly lower in hyperconfluent regions than in less confluent regions. Although this result is not consistent with the common finding that collective cell migration speed has an inverse correlation with cell density [42,47,48], the motion of the cells in the bands appears qualitatively different in that it is less persistent in direction and more fluctuating; indeed, the MSD is significantly lower in hyperconfluent regions than less confluent regions.

The progression of bands to hyperconfluency appears to be driven by cells migration to and joining aggregates rather than proliferation within the bands. EdU staining and cell morphological features in time-lapse videos show that proliferation occurs throughout the aggregates but is less prevalent within the hyperconfluent regions. Previous experiments with long EdU pulses (8 h) show EdU staining throughout similar constrained monolayers (mouse MSC cell line) with a decrease in proliferation with cell density [49]. In contrast, many studies of constrained epithelial monolayers report proliferation occurring predominantly at the edges corresponding to strong cell alignment and high traction forces [6,35,36]. Utilization of low Ca^{2+} media, shown to disrupt cell-cell interactions and subsequently the traction and cell alignment at the edges of cell aggregates [16,50], did not inhibit the alignment of cells into bands across our aggregates but did stop the bands from progressing to hyperconfluency and self-detachment. However, the results should be interpreted carefully as the initial cell alignment occurred in the 48 hours prior to depleting calcium from media (Fig. 5A), and decreased proliferation rates in low-calcium media may contribute to the lower cell density [37]. Regardless, the results demonstrate that removing calcium from the media does not reverse the local collective behavior or fully block VIC proliferation.

The hyperconfluent bands produce high, localized traction stresses at their endpoints. In contrast, in previous studies with confluent islands of epithelial cells and cell lines that are not highly motile [51], traction stresses are highest and roughly uniform at the edges, and the predicted cell-layer stresses increase from the edge to the center [9,10,25,52,53]. Time-lapse TFM heatmaps demonstrate that the magnitudes of traction stress vary with time but are consistently located at band endpoints and are directed inward indicating high traction forces at each end. Traction stresses increase as bands progress from confluent to hyper-

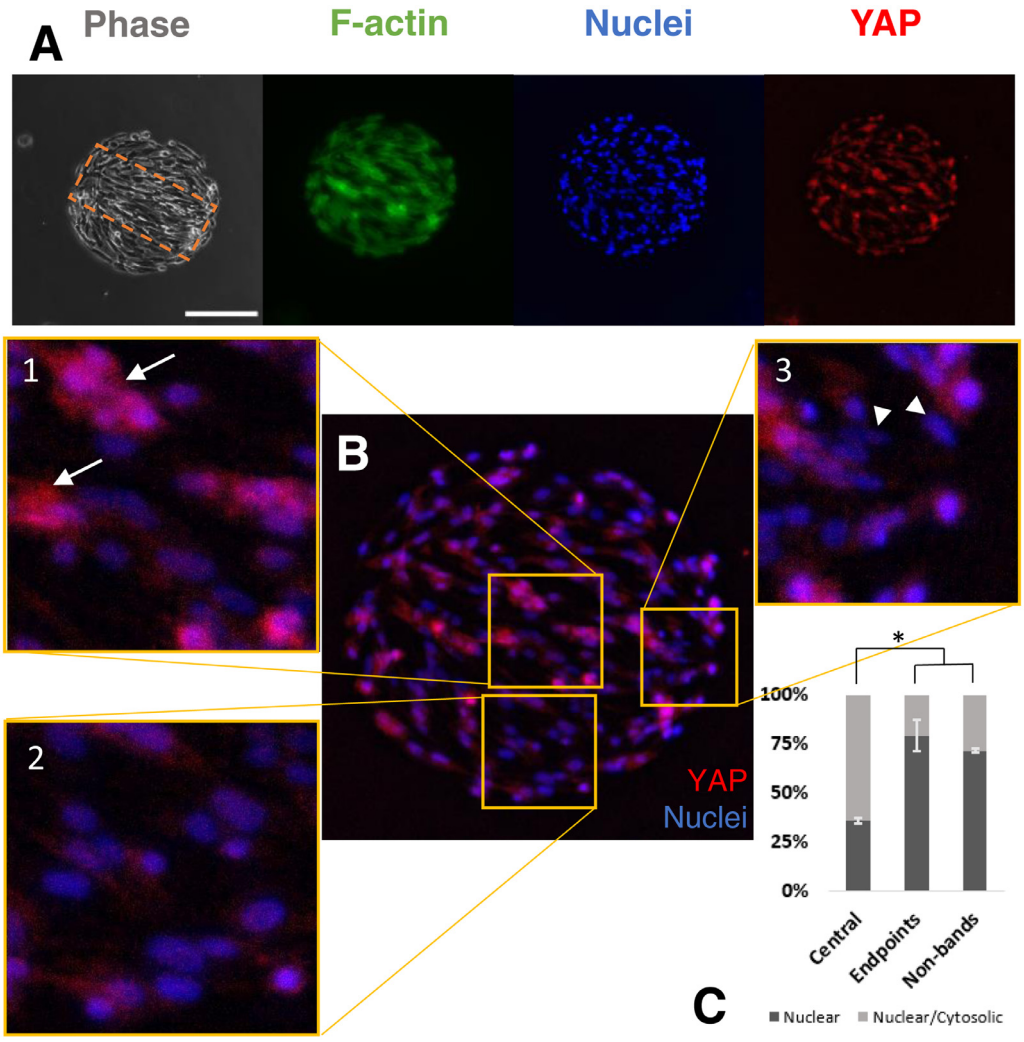

Fig. 7. A greater proportion of cytosolic YAP is observed in the center of hyperconfluent bands than at the ends. A) Phase image of fixed, permeabilized, fluorescent images of F-actin, nuclei, and YAP in a hyperconfluent aggregate exhibiting banding (dashed orange box). B) YAP/Hoechst merged image shows mixed cytosolic/nuclear YAP in the hyperconfluent center (inset 1), outside of the band (inset 2), and nuclear YAP at the endpoint of the band (inset 3). Arrows point to examples of cytosolic/nuclear YAP, and arrowheads point to examples of nuclear YAP. C) . * $p < 0.001$ from two-way ANOVA, $n = 615$ cells from 4 aggregates. Scale bar = 200 μm.

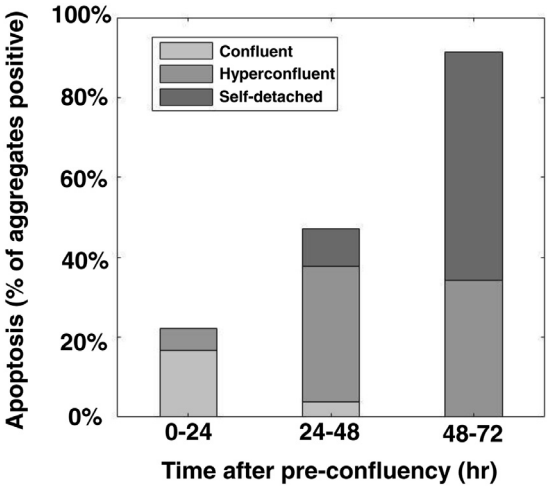

Fig. 8. Apoptosis increases with culture time. A small proportion of confluent aggregates have apoptotic cells at the early timepoint, whereas as the majority of aggregates become hyperconfluent and self-detached an increasing proportion exhibit apoptosis ($n = 53$ aggregates).

confluent and eventually lead to the detachment of portions of the aggregates from the substrate when the collagen/substrate bond strength is exceeded.

Despite the high total force at the ends of the bands, the biological markers examined suggest a low stress environment inside of the bands (as discussed below). Unfortunately, it is not feasible to calculate the stress or force per cell in the bands as they are not uniaxial cables attached only at the ends. The interactions with the adjacent cells are not known and there are additional (albeit low magnitude) traction stresses below the bands. In theory, monolayer stress microscopy (MSM) could be used to calculates the in-plane stresses of the cells throughout the aggregate from the traction stress maps; however, MSM assumes homogenous contractile and mechanical properties throughout the cell layer. We have previously shown that these calculations are not accurate for heterogeneous cell aggregates without incorporating the local cell properties which are not known for the banded aggregates [22].

Cells in hyperconfluent regions have smaller areas and cytosolic YAP; markers that are characteristic of cells in low-stress environments such as when cultured on soft substrates or on small protein islands that constrain spreading [25,26,54,55]. In contrast, cells at band endpoints have more nucleated YAP similar to that observed for single cells on unpatterned stiff substrates [56] and for con-

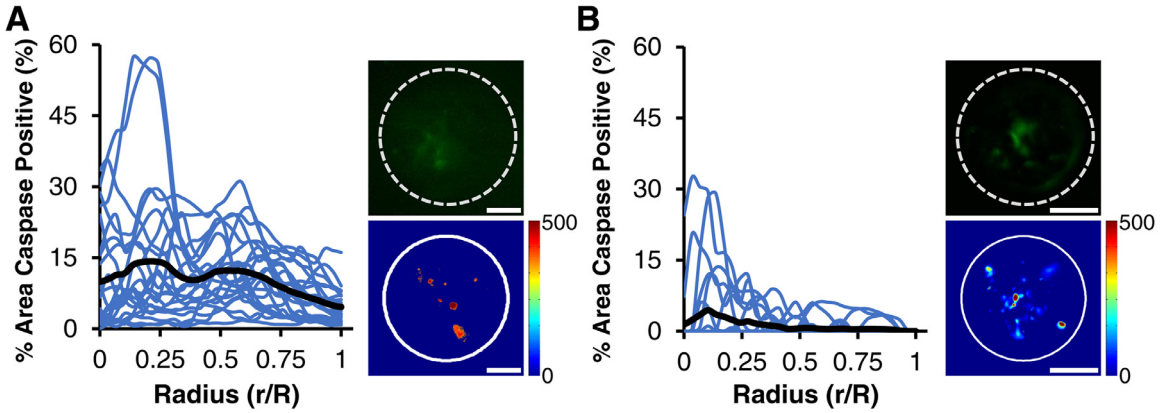

Fig. 9. Apoptosis is decreased significantly by YAP activation. A) The portion of aggregates positive for caspase in control VICs decreases from the center to edge. Image of a single aggregate stained for cleaved caspase-3/7 (top inset; green, dotted line indicates aggregate edge) and heat map for average caspase-3/7 intensity (bottom inset, $n = 24$ aggregates from 3 replicates). B) The portion of aggregates positive for caspase in VICs with constitutively active YAP decreases from center to edge. Image of a single aggregate stained for cleaved caspase-3/7 (top inset; green, dotted line indicates aggregate edge) and heat map for average caspase-3/7 intensity (bottom inset, $n = 23$ aggregates from 3 replicates). Scale bar = 50 μm.

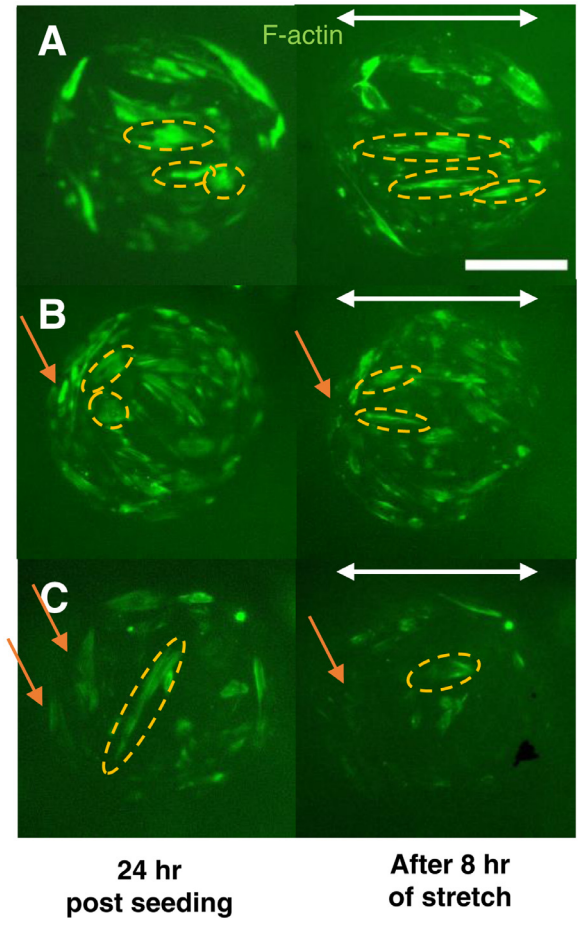

Fig. 10. Dynamic stretch reinforces F-actin alignment for cells in the direction of stretch and disrupts the cytoskeleton of cells aligned away from the stretch axis. A) Representative example of cells within a band roughly in the direction of stretch where the F-actin is intensified, and the cells are elongated after stretch. B) Representative example of cells within bands that are oriented within 45° of the stretch axis showing reorientation towards the direction of stretch. C) Representative example of a highly elongated cell within a band oriented greater than 45° from the stretch axis becoming more rounded and reorienting towards the stretch direction. Panels B and C also show that cells aligned along the edge perpendicular to the stretch direction retract (orange arrows). For all panels, F-actin of live VICs was stained with CellMask™ Actin before and after application of 10% uniaxial stretch for 8 h at 1 Hz; brightly stained cells inside of bands are outlined by ellipses to show change in orientation and elongation. Scale bar = 200 μm.

fluent primary fibroblasts on protein islands [16]. Apoptosis, which is also associated with low cell stress [57,58], increases as aggregates progress to hyperconfluency. Consistent with this result, almost every aggregate that can no longer generate substantial traction due to being partially detached from the substrate is caspase positive. As YAP enhances the transcription of pro-survival genes [27,59,60], we wondered if YAP plays a defining role in apoptosis in VICs. We found that constitutively activating YAP substantially decreases apoptosis consistent with findings from studies of epithelial cell lines [61]. While high traction stresses measured at the ends of the bands seem contradictory with low stress within the bands, it is possible that the high force in the band is generated/transmitted by many cells in parallel, i.e., high total force but low force per cell. This interpretation is consistent with our computational model of circular cell aggregates with radially increasing contractility from the center to the edge which predicts low stress in the central region despite high traction stresses transmitted to the substrate at the edges [22].

To further investigate the state of stress in the bands, we applied cyclic uniaxial stretch to confluent aggregates. Under the assumption that cells attempt to reach a homeostatic stress level [62], we postulated that if cells within the bands were under high tension, they would reorient away from stretch to regain their preferred stress level, whereas if cells were confined due to high cell density and not able to generate their preferred level of homeostatic tension, they would spread out and reorient towards stretch. Isolated VICs [30] and other fibroblasts cultured on stiff substrates exhibit strain avoidance [63–66] as do epithelial/endothelial sheets [67,68]. In contrast, when cells are cultured on collagen gels [69], within low density soft collagen gels [70,71] or when contractility is inhibited [68], cells reorient towards stretch. Consistent with the low stress interpretation, we observed that VICs within bands that are already oriented towards the direction of stretch elongate and have more pronounced and aligned cytoskeletal arrangement, whereas cells within bands roughly perpendicular to stretch retracted or reoriented towards the direction of stretch. We did not observe increased aggregate detachment with stretch which also suggests low stress in the aggregates. Cyclic (equibiaxial) stretch of VIC monolayers, in combination with TGF-beta treatment, has been shown to potentiate cell detachment and formation of aggregates [72]. As we presumed that edge cells were under relatively high circumferential stress due to their elongated morphology and based on computational model predictions of high circumferential stresses at the edges of constrained monolayers [7], we expected

these cells to reorient away from the stretch direction. Instead, we observed that the cells which were parallel to the direction of stretch maintained their elongation, and cells that were perpendicular to the direction of stretch retracted and/or reoriented away from the stretch direction. Cyclically stretched epithelial (MDCK) cells have been shown to increase their polarization (aspect ratio) when aligned around a "wound" edge in a monolayer model with a hole (essentially the inverse of our "island" system) consistent with the behavior we observe for cells aligned with the stretch axis, but the retraction of edge cells perpendicular to stretch has not been reported [73]. It is possible that the aligned bands in our system disrupt the emergent radial-symmetric stress field resulting in relatively low stress in edge cells, thus these cells reorient in the stretch direction to increase their stress towards a homeostatic level or to minimize shear stress [74].

5. Conclusion

Our results indicate that cell alignment and subsequent local collective behavior leads to substantial heterogeneity between and within constrained monolayers of primary fibroblastic cells. Multicellular bands are formed by cell-cell interactions locally. As cells become more dense within the bands, YAP becomes excluded from the nucleus and apoptotic rates increase. These findings suggest that strong local cell-cell interactions between primary fibroblastic cells can disrupt the global collective cellular behavior; this local collective cell behavior may play an important role in development and disease of connective tissues.

The findings of this research are specifically crucial in the biology of VICs, as there is less information on their behavior compared to other cell types such as epithelial cells and fibroblast/myoblast cell lines. The mechanical environment of VICs is hypothesized to contribute to diseases such as calcification. In this research, we showed that emergent behavior arising from cell-cell interactions may be as important as the external mechanical environment of VICs on their behavior.

Declaration of Competing Interest

The authors declare that they have no known competing financial interests or personal relationships that could have appeared to influence the work reported in this paper.

Acknowledgments

We would like to thank Sabine Hahn for her help editing the manuscript, Seyed Mohammad Jafar Sobhani for his help with graphical plotting with MATLAB, Milad Saadat for his help in visualization of data, as well as Marsha Rolle and CERES labs located in Worcester Polytechnic Institute for use of the Cytation microscope and George Pins for donation of neonatal human dermal fibroblastic cells. This work was funded in part by the American Heart Association (20AIREA35120448) and the National Science Foundation (CMMI 1761432).

Supplementary materials

Supplementary material associated with this article can be found, in the online version, at doi:10.1016/j.actbio.2022.10.041.

References

[1] M. Vishwakarma, B. Thurakkal, J.P. Spatz, T. Das, Dynamic heterogeneity influences the leader–follower dynamics during epithelial wound closure, Philos. Trans. R. Soc. B 375 (1807) (2020) 20190391.
[2] B.N. Nanavati, A.S. Yap, J.L. Teo, Symmetry breaking and epithelial cell extrusion, Cells 9 (6) (2020).
[3] X. Trepat, J.J. Fredberg, Plithotaxis and emergent dynamics in collective cellular migration, Trends Cell Biol. 21 (11) (2011) 638–646.
[4] B.A. Camley, W.-J. Rappel, Physical models of collective cell motility: from cell to tissue, J. Phys. D 50 (11) (2017) 113002.
[5] B. Ladoux, R.-M. Mège, Mechanobiology of collective cell behaviours, Nat. Rev. Mol. Cell Biol. 18 (12) (2017) 743–757.
[6] S.J. Streichan, C.R. Hoerner, T. Schneidt, D. Holzer, L. Hufnagel, Spatial constraints control cell proliferation in tissues, Proc. Nat. Acad. Sci. U.S.A. 111 (15) (2014) 5586–5591.
[7] S. He, C. Liu, X. Li, S. Ma, B. Huo, B. Ji, Dissecting collective cell behavior in polarization and alignment on micropatterned substrates, Biophys. J. 109 (3) (2015) 489–500.
[8] M.R. Ng, A. Besser, J.S. Brugge, G. Danuser, Mapping the dynamics of force transduction at cell–cell junctions of epithelial clusters, Elife 3 (2014) e03282.
[9] C.M. Nelson, R.P. Jean, J.L. Tan, W.F. Liu, N.J. Sniadecki, A.A. Spector, C.S. Chen, Emergent patterns of growth controlled by multicellular form and mechanics, Proc. Nat. Acad. Sci. U.S.A. 102 (33) (2005) 11594–11599.
[10] B. Li, F. Li, K.M. Puskar, J.H. Wang, Spatial patterning of cell proliferation and differentiation depends on mechanical stress magnitude, J. Biomech. 42 (11) (2009) 1622–1627.
[11] X. Trepat, M.R. Wasserman, T.E. Angelini, E. Millet, D.A. Weitz, J.P. Butler, J.J. Fredberg, Physical forces during collective cell migration, Nat. Phys. 5 (6) (2009) 426–430.
[12] M. Moussus, C.d. Loughian, D. Fuard, M. Courçon, D. Gulino-Debrac, H. Delanoë-Ayari, A. Nicolas, Intracellular stresses in patterned cell assemblies, Soft Matter 10 (14) (2014) 2414–2423.
[13] M. Uroz, S. Wistorf, X. Serra-Picamal, V. Conte, M. Sales-Pardo, P. Roca-Cusachs, R. Guimerà, X. Trepat, Regulation of cell cycle progression by cell–cell and cell–matrix forces, Nat. Cell Biol. 20 (6) (2018) 646–654.
[14] T.P.J. Wyatt, A.R. Harris, M. Lam, Q. Cheng, J. Bellis, A. Dimitracopoulos, A.J. Kabla, G.T. Charras, B. Baum, Emergence of homeostatic epithelial packing and stress dissipation through divisions oriented along the long cell axis, Proc. Natl. Acad. Sci. 112 (18) (2015) 5726–5731.
[15] J. Paek, J.W. Song, E. Ban, Y. Morimitsu, C.O. Osuji, V.B. Shenoy, D.D. Huh, Soft robotic constrictor for in vitro modeling of dynamic tissue compression, Sci. Rep. 11 (1) (2021) 16478.
[16] T. Xie, S.R. St Pierre, N. Olaranont, L.E. Brown, M. Wu, Y. Sun, Condensation tendency and planar isotropic actin gradient induce radial alignment in confined monolayers, Elife 10 (2021) e60381.
[17] G. Duclos, C. Erlenkämper, J.-F. Joanny, P. Silberzan, Topological defects in confined populations of spindle-shaped cells, Nat. Phys. 13 (1) (2017) 58–62.
[18] Y. Yip Cindy Ying, J.-H. Chen, R. Zhao, A. Simmons Craig, Calcification by valve interstitial cells is regulated by the stiffness of the extracellular matrix, Arterioscler. Thromb. Vasc. Biol. 29 (6) (2009) 936–942.
[19] M. Bogdanova, A. Zabirnyk, A. Malashicheva, K.Z. Enayati, T.A. Karlsen, M.-L. Kaljusto, J.-P.E. Kvitting, E. Dissen, G.J. Sullivan, A. Kostareva, K.-O. Stensløkken, A. Rutkovskiy, J. Vaage, Interstitial cells in calcified aortic valves have reduced differentiation potential and stem cell-like properties, Sci. Rep. 9 (1) (2019) 12934.
[20] B. Jian, N. Narula, Q.-y. Li, E.R. Mohler, R.J. Levy, Progression of aortic valve stenosis: TGF-β1 is present in calcified aortic valve cusps and promotes aortic valve interstitial cell calcification via apoptosis, Ann. Thorac. Surg. 75 (2) (2003) 457–465.
[21] H.A. Cirka, J. Uribe, V. Liang, F.J. Schoen, K.L. Billiar, Reproducible in vitro model for dystrophic calcification of cardiac valvular interstitial cells: insights into the mechanisms of calcific aortic valvular disease, Lab. Chip 17 (5) (2017) 814–829.
[22] Z.E. Goldblatt, H. Ashouri Choshali, H.A. Cirka, V. Liang, Q. Wen, D. McCollum, N. Rahbar, K.L. Billiar, Heterogeneity profoundly alters emergent stress fields in constrained multicellular systems, Biophys. J. 118 (1) (2020) 15–25.
[23] H. Ashouri Choshali, K.L. Billiar, N. Rahbar, Anisotropy profoundly alters stress fields within contractile cells and cell aggregates, Biomech. Model. Mechanobiol. (2022).
[24] A. Das, R.S. Fischer, D. Pan, C.M. Waterman, YAP nuclear localization in the absence of cell-cell contact is mediated by a filamentous actin-dependent, Myosin II- and Phospho-YAP-independent pathway during extracellular matrix mechanosensing, J. Biol. Chem. 291 (12) (2016) 6096–6110.
[25] M. Aragona, T. Panciera, A. Manfrin, S. Giulitti, F. Michielin, N. Elvassore, S. Dupont, S. Piccolo, A mechanical checkpoint controls multicellular growth through YAP/TAZ regulation by actin-processing factors, Cell 154 (5) (2013) 1047–1059.
[26] F. Calvo, N. Ege, A. Grande-Garcia, S. Hooper, R.P. Jenkins, S.I. Chaudhry, K. Harrington, P. Williamson, E. Moeendarbary, G. Charras, E. Sahai, Mechanotransduction and YAP-dependent matrix remodelling is required for the generation and maintenance of cancer-associated fibroblasts, Nat. Cell Biol. 15 (6) (2013) 637–646.
[27] V.A. Codelia, G. Sun, K.D. Irvine, Regulation of YAP by mechanical strain through Jnk and Hippo signaling, Curr. Biol. 24 (17) (2014) 2012–2017.
[28] A.M. Kloxin, J.A. Benton, K.S. Anseth, In situ elasticity modulation with dynamic substrates to direct cell phenotype, Biomaterials 31 (1) (2010) 1–8.
[29] H. Wang, S.M. Haeger, A.M. Kloxin, L.A. Leinwand, K.S. Anseth, Redirecting valvular myofibroblasts into dormant fibroblasts through light-mediated reduction in substrate modulus, PLoS One 7 (7) (2012) p. e39969-e39969.
[30] H. Cirka, M. Monterosso, N. Diamantides, J. Favreau, Q. Wen, K. Billiar, Active traction force response to long-term cyclic stretch is dependent on cell pre-stress, Biophys. J. 110 (8) (2016) 1845–1857.

[31] R.A. Gould, J.T. Butcher, Isolation of valvular endothelial cells, J. Vis. Exp. (46) (2010) 2158.
[32] V. Voccoli, I. Tonazzini, G. Signore, M. Caleo, M. Cecchini, Role of extracellular calcium and mitochondrial oxygen species in psychosine-induced oligodendrocyte cell death, Cell Death. Dis. 5 (11) (2014) p. e1529-e1529.
[33] S. Dutta, S. Mana-Capelli, M. Paramasivam, I. Dasgupta, H. Cirka, K. Billiar, D. McCollum, TRIP6 inhibits Hippo signaling in response to tension at adherens junctions, EMBO Rep. 19 (2) (2018) 337–350.
[34] H. Ma, A.R. Killaars, F.W. DelRio, C. Yang, K.S. Anseth, Myofibroblastic activation of valvular interstitial cells is modulated by spatial variations in matrix elasticity and its organization, Biomaterials 131 (2017) 131–144.
[35] B.B. Silver, A.E. Wolf, J. Lee, M.-F. Pang, C.M. Nelson, Epithelial tissue geometry directs emergence of bioelectric field and pattern of proliferation, Mol. Biol. Cell 31 (16) (2020) 1691–1702.
[36] B. Li, F. Li, H.X. Li, X.C. Xu, M. Szczodry, Z.C. Yang, J.S. Lin, J.H.C. Wang, Cellular mechanical stress gradient regulates cell proliferation and differentiation patterns, Mol. Cell. Biomech. 3 (4) (2006).
[37] C.R. Kahl, A.R. Means, Regulation of cell cycle progression by calcium/calmodulin-dependent pathways, Endocr. Rev. 24 (6) (2003) 719–736.
[38] A. Chansard, N. Dubrulle, M. Poujol de Molliens, P.B. Falanga, T. Stephen, M. Hasan, G. van Zandbergen, N. Aulner, S.L. Shorte, B. David-Watine, Unveiling interindividual variability of human fibroblast innate immune response using robust cell-based protocols, Front. Immunol. 11 (2021) p. 569331-569331.
[39] M.A. Carlson, A.K. Prall, J.J. Gums, A. Lesiak, V.K. Shostrom, Biologic variability of human foreskin fibroblasts in 2D and 3D culture: implications for a wound healing model, BMC Res. Notes 2 (1) (2009) 229.
[40] M.D. Lynch, F.M. Watt, Fibroblast heterogeneity: implications for human disease, J. Clin. Invest. 128 (1) (2018) 26–35.
[41] C. Pérez-González, R. Alert, C. Blanch-Mercader, M. Gómez-González, T. Kolodziej, E. Bazellieres, J. Casademunt, X. Trepat, Active wetting of epithelial tissues, Nat Phys 15 (1) (2019) 79–88.
[42] K. Doxzen, S.R.K. Vedula, M.C. Leong, H. Hirata, N.S. Gov, A.J. Kabla, B. Ladoux, C.T. Lim, Guidance of collective cell migration by substrate geometry, Integr. Biol. 5 (8) (2013) 1026–1035.
[43] C.A. Reinhart-King, M. Dembo, D.A. Hammer, The dynamics and mechanics of endothelial cell spreading, Biophys. J. 89 (1) (2005) 676–689.
[44] S. Garcia, E. Hannezo, J. Elgeti, J.-F. Joanny, P. Silberzan, S. Gov Nir, Physics of active jamming during collective cellular motion in a monolayer, Proc. Natl. Acad. Sci. 112 (50) (2015) 15314–15319.
[45] L. Atia, D. Bi, Y. Sharma, J.A. Mitchel, B. Gweon, S. Koehler, S.J. DeCamp, B. Lan, J.H. Kim, R. Hirsch, A.F. Pegoraro, K.H. Lee, J.R. Starr, D.A. Weitz, A.C. Martin, J.A. Park, J.P. Butler, J.J. Fredberg, Geometric constraints during epithelial jamming, Nat. Phys. 14 (2018) 613–620.
[46] D.K. Vig, A.E. Hamby, C.W. Wolgemuth, Cellular contraction can drive rapid epithelial flows, Biophys. J. 113 (7) (2017) 1613–1622.
[47] S.-Z. Lin, W.-Y. Zhang, D. Bi, B. Li, X.-Q. Feng, Energetics of mesoscale cell turbulence in two-dimensional monolayers, Commun. Phys. 4 (1) (2021) 21.
[48] B. Li, Sean X. Sun, Coherent motions in confluent cell monolayer sheets, Biophys. J. 107 (7) (2014) 1532–1541.
[49] Z.T. Berent, I. Jain, G.H. Underhill, A.J. Wagoner Johnson, Simulated confluence on micropatterned substrates correlates responses regulating cellular differentiation, Biotechnol. Bioeng. 119 (6) (2022) 1641–1659.
[50] V. Maruthamuthu, B. Sabass, U.S. Schwarz, M.L. Gardel, Cell-ECM traction force modulates endogenous tension at cell-cell contacts, Proc. Nat. Acad. Sci. U.S.A. 108 (12) (2011) 4708–4713.
[51] E.N. Schaumann, M.F. Staddon, M.L. Gardel, S. Banerjee, Force localization modes in dynamic epithelial colonies, Mol. Biol. Cell 29 (23) (2018) 2835–2847.
[52] A. Deglincerti, F. Etoc, M.C. Guerra, I. Martyn, J. Metzger, A. Ruzo, M. Simunovic, A. Yoney, A.H. Brivanlou, E. Siggia, A. Warmflash, Self-organization of human embryonic stem cells on micropatterns, Nat. Protoc. 11 (11) (2016) 2223–2232.
[53] R. Tran, C. Moraes, C. Hoesli, Controlled clustering enhances PDX1 and NKX6.1 expression in pancreatic endoderm cells derived from pluripotent stem cells, Sci. Rep. 10 (2020) 1190.
[54] K.-I. Wada, K. Itoga, T. Okano, S. Yonemura, H. Sasaki, Hippo pathway regulation by cell morphology and stress fibers, Development 138 (18) (2011) 3907–3914.
[55] S. Mascharak, P.L. Benitez, A.C. Proctor, C.M. Madl, K.H. Hu, R.E. Dewi, M.J. Butte, S.C. Heilshorn, YAP-dependent mechanotransduction is required for proliferation and migration on native-like substrate topography, Biomaterials 115 (2017) 155–166.
[56] S. Dupont, L. Morsut, M. Aragona, E. Enzo, S. Giulitti, M. Cordenonsi, F. Zanconato, J. Le Digabel, M. Forcato, S. Bicciato, N. Elvassore, S. Piccolo, Role of YAP/TAZ in mechanotransduction, Nature 474 (7350) (2011) 179–183.
[57] M. Egerbacher, S.P. Arnoczky, O. Caballero, M. Lavagnino, K.L. Gardner, Loss of homeostatic tension induces apoptosis in tendon cells: an in vitro study, Clin. Orthop. Relat. Res. 466 (7) (2008) 1562–1568.
[58] J.D. Humphrey, E.R. Dufresne, M.A. Schwartz, Mechanotransduction and extracellular matrix homeostasis, Nat Rev. Mol. Cell Biol. 15 (12) (2014) 802–812.
[59] H. Zhang, H.A. Pasolli, E. Fuchs, Yes-associated protein (YAP) transcriptional coactivator functions in balancing growth and differentiation in skin, Proc. Nat. Acad. Sci. U.S.A. 108 (6) (2011) 2270–2275.
[60] Z. Lin, P. Zhou, A. von Gise, F. Gu, Q. Ma, J. Chen, H. Guo, P.R.R. van Gorp, D.-Z. Wang, W.T. Pu, Pi3kcb links Hippo-YAP and PI3K-AKT signaling pathways to promote cardiomyocyte proliferation and survival, Circ. Res. 116 (1) (2015) 35–45.
[61] Y. Liu, K. He, Y. Hu, X. Guo, D. Wang, W. Shi, J. Li, J. Song, YAP modulates TGF-β1-induced simultaneous apoptosis and EMT through upregulation of the EGF receptor, Sci. Rep. 7 (1) (2017) 45523.
[62] R.A. Brown, R. Prajapati, D.A. McGrouther, I.V. Yannas, M. Eastwood, Tensional homeostasis in dermal fibroblasts: Mechanical responses to mechanical loading in three-dimensional substrates, J. Cell. Physiol. 175 (3) (1998) 323–332.
[63] J.H.C. Wang, P. Goldschmidt-Clermont, J. Wille, F.C.P. Yin, Specificity of endothelial cell reorientation in response to cyclic mechanical stretching, J. Biomech. 34 (12) (2001) 1563–1572.
[64] Y. Shao, X. Tan, R. Novitski, M. Muqaddam, P. List, L. Williamson, J. Fu, A.P. Liu, Uniaxial cell stretching device for live-cell imaging of mechanosensitive cellular functions, Rev. Sci. Instrum. 84 (11) (2013) p. 114304-114304.
[65] T. Ristori, T.M.W. Notermans, J. Foolen, N.A. Kurniawan, C.V.C. Bouten, F.P.T. Baaijens, S. Loerakker, Modelling the combined effects of collagen and cyclic strain on cellular orientation in collagenous tissues, Sci. Rep. 8 (1) (2018) 8518.
[66] A. Greiner, H. Chen, J. Spatz, R. Kemkemer, Cyclic tensile strain controls cell shape and directs actin stress fiber formation and focal adhesion alignment in spreading cells, PLoS One 8 (2013) e77328.
[67] L. Gérémie, E. Ilker, M. Bernheim-Dennery, C. Cavaniol, J.-L. Viovy, D.M. Vignjevic, J.-F. Joanny, S. Descroix, Evolution of a confluent gut epithelium under on-chip cyclic stretching, Phys. Rev. Res. 4 (2) (2022) 023032.
[68] R. Kaunas, P. Nguyen, S. Usami, S. Chien, Cooperative effects of Rho and mechanical stretch on stress fiber organization, Proc. Natl. Acad. Sci. 102 (44) (2005) 15895–15900.
[69] A. Tondon, R. Kaunas, The direction of stretch-induced cell and stress fiber orientation depends on collagen matrix stress, PLoS One 9 (2) (2014) e89592.
[70] C. Sears, R. Kaunas, The many ways adherent cells respond to applied stretch, J. Biomech. 49 (8) (2016) 1347–1354.
[71] J. Foolen, M.W.J.T. Janssen-van den Broek, F.P.T. Baaijens, Synergy between Rho signaling and matrix density in cyclic stretch-induced stress fiber organization, Acta Biomater. 10 (5) (2014) 1876–1885.
[72] C.I. Fisher, J. Chen, W.D. Merryman, Calcific nodule morphogenesis by heart valve interstitial cells is strain dependent, Biomech. Model. Mechanobiol. 1 (2012).
[73] J. Xu, X. Xu, X. Li, S. He, D. Li, B. Ji, Cellular mechanics of wound formation in single cell layer under cyclic stretching, Biophys. J. 121 (2) (2022) 288–299.
[74] C. Liu, S. He, X. Li, B. Huo, B. Ji, Mechanics of cell mechanosensing on patterned substrate, J. Appl. Mech. 83 (5) (2016) 051014.